Microstructure, formation mechanism and properties of plasma-sprayed Cr$_7$C$_3$−CrSi$_2$−Al$_2$O$_3$ coatings

Yu-duo MA[1], Pei-wen RU[1], Lei WANG[1], Yong YANG[1], Peng-yue GAO[1],
Yan-wei WANG[1], Yu-hang CUI[1], Wen-wei SUN[1], Xing-yu WANG[1], Liang WANG[2]

1. Key Laboratory for New Type of Functional Materials in Hebei Province,
School of Materials Science and Engineering,
State Key Laboratory of Reliability and Intelligence of Electrical Equipment,
Tianjin Key Laboratory of Materials Laminating Fabrication and Interface Control Technology,
Hebei University of Technology, Tianjin 300401, China;
2. Integrated Computational Materials Research Centre, Shanghai Institute of Ceramics,
Chinese Academy of Sciences, Shanghai 201899, China

Abstract: The Cr$_7$C$_3$−CrSi$_2$−Al$_2$O$_3$ composite coatings were prepared by plasma spraying Cr$_7$C$_3$−CrSi$_2$−Al$_2$O$_3$ and Al−Cr$_2$O$_3$−SiC composite powders, respectively. The microstructure, formation mechanism and properties of the two Cr$_7$C$_3$−CrSi$_2$−Al$_2$O$_3$ composite coatings obtained by plasma spraying were investigated, and the reaction mechanism of the Al−Cr$_2$O$_3$−SiC system was explored. The results show that the coating obtained by plasma spraying Al−Cr$_2$O$_3$−SiC composite powders had thinner lamella and more tortuous interlayer interface, and the in-situ synthesized Cr$_7$C$_3$, CrSi$_2$ and Al$_2$O$_3$ in the coating were all nano-crystallines. Compared with the Cr$_7$C$_3$−CrSi$_2$−Al$_2$O$_3$ coating prepared by plasma spraying Cr$_7$C$_3$−CrSi$_2$−Al$_2$O$_3$ composite powders, the plasma-sprayed Cr$_7$C$_3$−CrSi$_2$−Al$_2$O$_3$ coating obtained from Al−Cr$_2$O$_3$−SiC composite powders had higher density, higher microhardness (increased by 20%), better fracture toughness and lower wear rate (reduced by 28%).

Key words: plasma spraying; in-situ synthesis; nanostructure; strengthening and toughening; wear resistance

1 Introduction

Cr$_7$C$_3$ ceramic has good wear resistance, corrosion resistance and oxidation resistance, so it is expected to provide effective surface protection for various workpieces to resist harsh working conditions [1]. However, due to the high melting point of Cr$_7$C$_3$ ceramics, currently prepared pure Cr$_7$C$_3$ coatings have problems such as high porosity, high brittleness, and poor performance. Adding low-melting point substances to Cr$_7$C$_3$ ceramics can not only reduce the porosity and brittleness of the coating, but also improve the performance of the resulting composite coating [2−4]. The melting point of CrSi$_2$ is relatively low, and the SiO$_2$ film formed in a high-temperature oxidizing atmosphere can have a self-sealing effect on the coating [5,6]. LIU et al [7] introduced CrSi$_2$ ceramics used as additives into ZrSi$_2$−Y$_2$O$_3$ coating to suppress the development of microcracks and reduce the porosity of the coating. Al$_2$O$_3$ is widely used as a reinforcing material for composite materials due to its high hardness, high strength and strong creep resistance below 1200 °C [8,9]. The preparation of high-quality and high-performance Cr$_7$C$_3$−CrSi$_2$−

Al_2O_3 composite coating is of great significance for protecting the substrate under wear, high-temperature and corrosion conditions.

Among the coating preparation methods, plasma spraying technology has become the most commonly used method for preparing composite coatings due to its simple and convenient process, high efficiency and controllable coating thickness [10−12]. As we all know, nanostructured ceramic materials have high mechanical and thermodynamic properties due to their quantum size and surface effects. However, due to the inherent interface mismatch defects between Cr_7C_3, $CrSi_2$ and Al_2O_3 and easy growth of grains at high temperatures, it is an arduous challenge to prepare high-strength and high-toughness nanostructured ceramic coatings by direct plasma spraying of target raw materials. The strategy of in-situ synthesis is considered promising because it can produce small-sized and uniformly-dispersed composite materials, while having a pollution-free interface and high thermodynamic stability [13−15]. In addition, the preparation of composite coating by the reactive synthesis method can avoid the problem that ceramic materials are difficult to melt.

In our previous work, the plasma-sprayed $Cr_7C_3−CrSi_2$ coating was obtained by Cr−SiC powder [16]. However, since the reaction of Cr and SiC is a non-self-propagating reaction, the continuous reaction of Cr and SiC requires constant heat from the outside. In addition, the large and irregular raw material Cr directly affects the reaction rate of Cr and SiC. Therefore, the thermite reaction is introduced to improve the reaction degree of Cr and SiC. ZHANG et al [17] synthesized a plasma-sprayed ZrB_2-based coating by $Al−B_2O_3−ZrO_2$ powder and the as-prepared coating had high toughness. XU et al [18] utilized Al, TiO_2 and B_4C as starting materials to synthesize $Al_2O_3−TiB_2−TiC/Al$ composite material. The hardness of the as-prepared $Al_2O_3−TiB_2−TiC/Al$ material was significantly increased. However, there is less report on the preparation of plasma-sprayed $Cr_7C_3−CrSi_2−Al_2O_3$ coating derived from $Al−Cr_2O_3−SiC$ composite powders.

In the present investigation, two types of composite powders ($Cr_7C_3−CrSi_2−Al_2O_3$ and $Al−Cr_2O_3−SiC$) were used to prepare $Cr_7C_3−CrSi_2−Al_2O_3$ composite coatings via plasma spraying technology. Microstructure, formation mechanism and properties of the two $Cr_7C_3−CrSi_2−Al_2O_3$ composite coatings were investigated in detail.

2 Experimental

2.1 Materials and preparation method

TC4 and NiCrAlY were used as the substrate material and the bonding layer material, respectively. Commercially available Cr_7C_3 powder, $CrSi_2$ powder, Al_2O_3 powder, Cr_2O_3 powder, Al powder and SiC powder were used as raw materials. According to the reaction formula, the mass ratio of the raw materials in the composite powders was calculated:

$$34Al+17Cr_2O_3+12SiC=4Cr_7C_3+6CrSi_2+17Al_2O_3$$
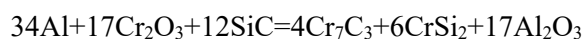
The raw materials with mass ratio of Cr_7C_3:$CrSi_2$:Al_2O_3 of 10:4:11 and Al:Cr_2O_3:SiC of 23:65:12 were spray-dried into $Cr_7C_3−CrSi_2−Al_2O_3$ and $Al−Cr_2O_3−SiC$ composite powders. The as-prepared $Cr_7C_3−CrSi_2−Al_2O_3$ and $Al−Cr_2O_3−SiC$ composite powders were deposited on the surface of the treated TC4 substrate by plasma spraying technology, respectively, to prepare composite coatings of about 250 μm in thickness. The 80 kW GP−80 spraying system equipped with 9M plasma gun was used to prepare coatings. The main plasma spraying parameters are as follows: the current was 500 A, the main gas (Ar) flow was 150 L/min, the secondary gas (H_2) flow was 30 L/min, the powder feeding gas flow rate was 4 L/min, and the spraying distance was 100 mm. A DTA/TG apparatus (DTA/TG 6300, Japan) was used for obtaining information about the reaction temperatures during the reactive process. The heating process is as follows: heating up to 1250 °C at a rate of 10 °C/min under an argon atmosphere. The $Al−Cr_2O_3−SiC$ composite powders were heat-treated by a tubular electric furnace with the same parameters as DTA/TG.

2.2 Materials characterization

The phase compositions of the composite powders and the composite coatings were defined by XRD (Rigaku DMAX−2500X), at a scanning speed of 4 (°)/min. The microstructure of the coatings and powders was characterized by scanning electron microscopy (HITACHI S−4800) and EDS. Image analysis method was used to quantify the porosity of coatings. The microscopic

morphology of the samples was observed by TEM (Tecnai G2 F30 S−TWIN, America), and the crystal structure of each phase in the sample was analyzed by selected area electron diffraction. The surface microhardness of the coatings was characterized by a microhardness tester (SHIMADZU HMV−2). The morphology of the indentations was observed with a scanning electron microscope to qualitatively analyze the toughness of the two coatings. An automatic scratch tester was used to test the scratch resistance of the coatings. A ball-on-disc tribometer (SFT−2M) was used to test the wear resistance of the coating. The Si_3N_4 ball with a diameter of 4 mm was used as counterpart. The normal load, loading time, rotation speed, and measuring method for tribological tests were set as 30 N, 10 min, 400 r/min, and cyclic friction, respectively. The wear rate of the coatings were calculated according to $W=V/(2\pi rntF)$, where V is the wear volume (mm^3), r is the distance from the center of the circle to the wear center (mm), n is the rotation speed (r/min), t is the loading time (min) and F is the load (N) [16].

3 Results and discussion

3.1 Phase composition and microstructure of composite coatings

From Fig. 1, the spray-dried Cr_7C_3−$CrSi_2$−Al_2O_3 composite powders were composed of Cr_7C_3, $CrSi_2$, Cr_3C_2, CrSi and α-Al_2O_3 phases. The Al−Cr_2O_3−SiC composite powders were composed of Cr_2O_3, SiC and Al phases. Phase compositions of the as-prepared Cr_7C_3−$CrSi_2$−Al_2O_3 coating were Cr_7C_3, $CrSi_2$, γ-Al_2O_3, α-Al_2O_3, Cr_3C_2, CrSi and Cr_2O_3. Phase compositions of the as-prepared Al−Cr_2O_3−SiC coating were Cr_7C_3, γ-Al_2O_3, $CrSi_2$, CrSi, Cr, Cr_2O_3 and SiC. By comparing Fig. 1(a) and Fig. 1(c), it can be seen that under the condition of plasma spraying, most of the chromium carbide and chromium silicides remained in the original phase, and only a small amount of chromium carbide and chromium silicide are oxidized to Cr_2O_3. At the same time, most of the α-Al_2O_3 phase is transformed into the γ-Al_2O_3 phase. The reason is that γ-Al_2O_3 with lower critical nucleation free
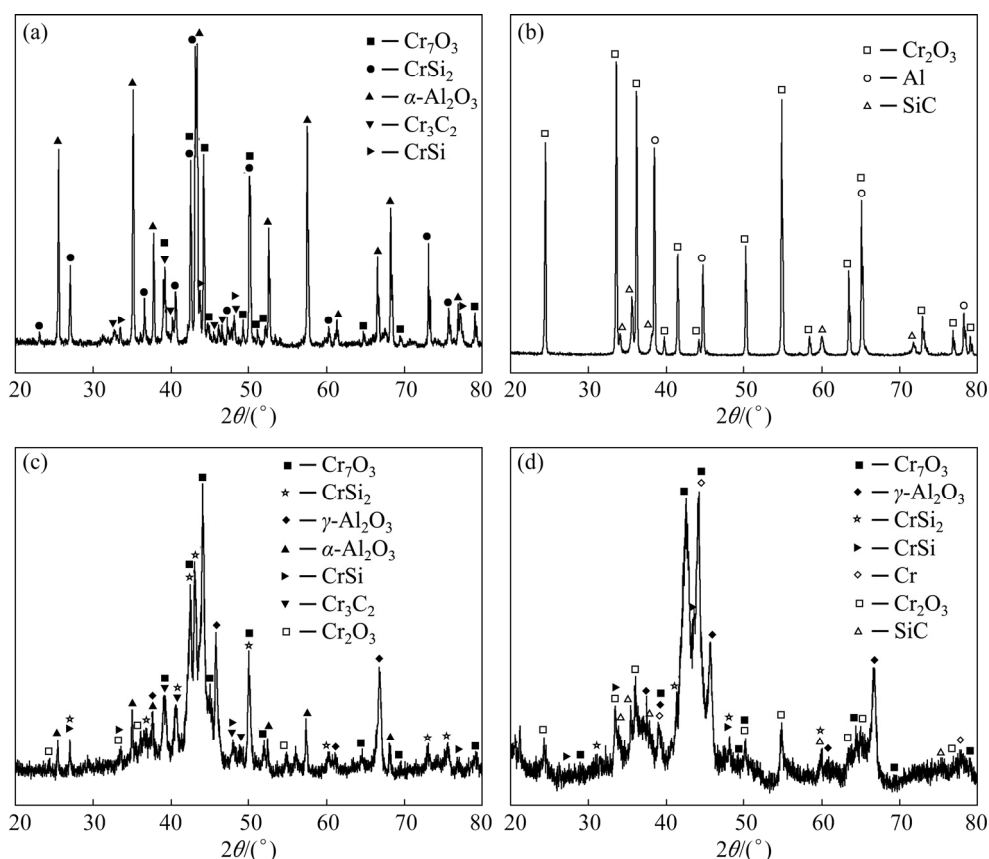

Fig. 1 X-ray diffraction patterns of composite powders and composite coatings: (a) Cr_7C_3−$CrSi_2$−Al_2O_3 composite powders; (b) Al−Cr_2O_3−SiC composite powders; (c) Cr_7C_3−$CrSi_2$−Al_2O_3 composite coating; (d) Al−Cr_2O_3−SiC composite coating

energy was easier to nucleate in the rapid solidification process of plasma spraying [19,20]. By comparing Figs. 1(b, d), it can be inferred that Cr_2O_3, SiC and Al reacted to form Cr_7C_3, $CrSi_2$, γ-Al_2O_3, CrSi and Cr phases during plasma spraying. The relative content of each phase in the two composite coatings was calculated based on the reference intensity ratio (RIR) of the characteristic peaks. The results show that the as-prepared Cr_7C_3−$CrSi_2$−Al_2O_3 coating contained Cr_7C_3 (43 wt.%), γ-Al_2O_3 (25 wt.%), α-Al_2O_3 (10 wt.%), $CrSi_2$ (9%), Cr_3C_2 (8 wt.%), Cr_2O_3 (3 wt.%) and CrSi (2 wt.%). The as-prepared Al−Cr_2O_3−SiC coating contained Cr_7C_3 (40 wt.%), γ-Al_2O_3 (24 wt.%), SiC (10 wt.%), Cr (10 wt.%), Cr_2O_3 (7 wt.%), CrSi (5 wt.%)) and $CrSi_2$ (4 wt.%).

From the cross-sectional SEM micrograph of the Cr_7C_3−$CrSi_2$−Al_2O_3 coating (Fig. 2(a)), it is found that the Cr_7C_3−$CrSi_2$−Al_2O_3 coating was well bonded to the substrate, but the Cr_7C_3−$CrSi_2$−Al_2O_3 coating has obvious large pores. The reason is that the Cr_7C_3−$CrSi_2$−Al_2O_3 composite powders were not sufficiently melted. From Fig. 2(b), the as-prepared Al−Cr_2O_3−SiC coating can be well combined with the substrate, and the Al−Cr_2O_3−SiC coating has no obvious large pores. The calculation results show that the porosity of the Al−Cr_2O_3−SiC coating (3.8%) is lower than that of the Cr_7C_3−$CrSi_2$−Al_2O_3 coating (8.5%). By comparing Figs. 2(c, d), the as-prepared Al−Cr_2O_3−SiC coating has thinner lamella and more tortuous interlayer interfaces. The reason may be that the Al−Cr_2O_3−SiC composite powders melted more fully, and therefore the Al−Cr_2O_3−SiC droplets had a better flattening degree after hitting the substrate. By combining XRD (Fig. 1), BSEM and EDS results (Table 1), the Area A was Al_2O_3 phase, Area B was mainly chromium carbide phase, Area C was chromium silicide phase, the white spherical particles (Area D) were Cr phases, Area E was mainly Al_2O_3 phase, Area F was mainly chromium carbide phase and Area G was mainly chromium silicide phase.

In order to further observe the morphology and distribution of the phases in the as-prepared Al−Cr_2O_3−SiC composite coating, the Al−Cr_2O_3−SiC composite coating was analyzed by TEM, and the results are shown in Fig. 3. In the electron diffraction pattern of the rod-shaped structure (Region A) in Fig. 3(a), the diffraction spots are elongated into stripes in a certain direction. This is an important feature of the Cr_7C_3 electron diffraction pattern. The length of the rod-shaped Cr_7C_3 produced by the reaction was about 200 nm and the width was about 30 nm. The microstructure of Region B in Fig. 3(b) was composed of $CrSi_2$
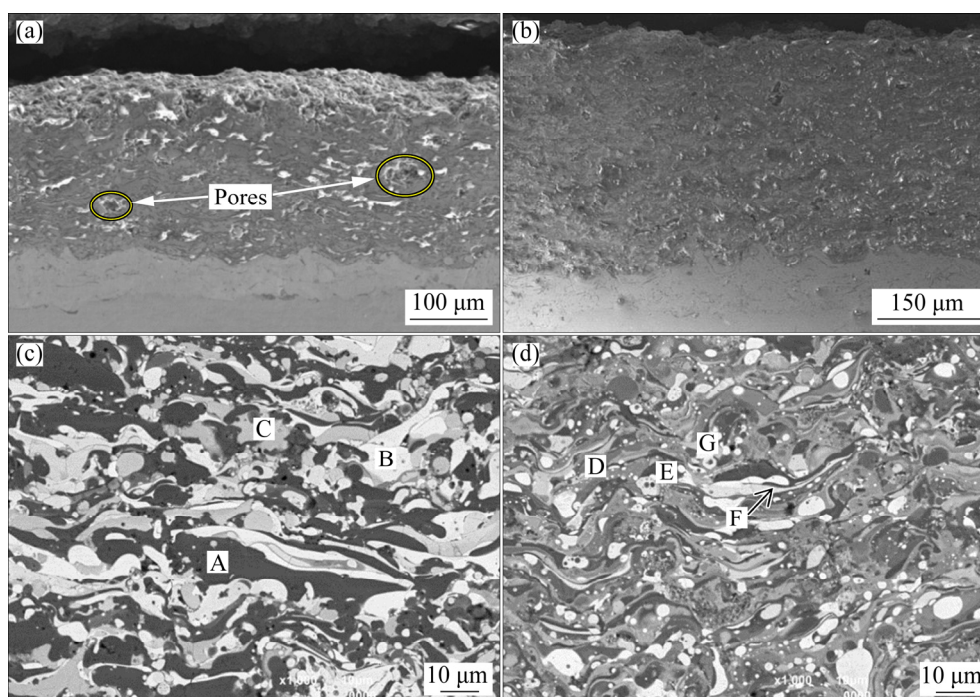

Fig. 2 Cross-sectional SEM (a, b) and BSE (c, d) micrographs of two composite coatings: (a, c) Cr_7C_3−$CrSi_2$−Al_2O_3; (b, d) Al−Cr_2O_3−SiC

Table 1 EDS analysis results of coatings (areas in Figs. 2(c, d) (wt.%)

Area	C	O	Al	Si	Cr
A	3.25	49.33	46.20	0.60	0.62
B	8.76	1.66	1.49	8.66	79.43
C	4.17	0.94	2.18	38.15	54.56
D	7.47	1.05	0.10	0.41	90.98
E	5.09	48.55	40.06	0.64	5.66
F	4.78	12.41	30.26	3.63	48.92
G	5.01	0.13	29.19	6.69	58.99

with hexagonal structure. The calibration result shows that the irregular sub-micron grains (Region C) in Fig. 3(c) were γ-Al_2O_3. The in-situ formed Cr_7C_3, $CrSi_2$ and γ-Al_2O_3 all exist in the Al−Cr_2O_3−SiC coating in the form of nanostructures.

The morphologies and corresponding SAED patterns of other phases in the Al−Cr_2O_3−SiC coating are shown in Fig. 4. The round crystal grains (Region A) in Fig. 4(a) were cubic Cr. The presentation of Cr in the coating was derived from the reaction between Al and Cr_2O_3. The reaction of Cr and SiC is an unsustainable reaction, and the continuous reaction of Cr and SiC requires

continuous external energy. Therefore, a small amount of Cr and SiC remain in the coating. The calibration result of columnar crystal (Region B) in Fig. 4(a) was Cr_2O_3. The Cr_2O_3 in the coating was left from the reaction of raw materials. The calibration result of Region C in Fig. 4(a) shows that it was amorphous phase, and the EDS analysis result of Region C shows that the amorphous phase mainly contained Al, Cr, and O elements.

3.2 Reaction process of Al−Cr_2O_3−SiC system and formation mechanism of composite coatings

3.2.1 Reaction process of Al−Cr_2O_3−SiC system

In order to understand the Al−Cr_2O_3−SiC reaction process, the Al−Cr_2O_3−SiC composite powders were analyzed by differential thermal and thermogravimetric analysis (DTA/TG). From the DTA curve in Fig. 5, there was an endothermic peak at 660 °C, which is considered to be the melting of Al [21]. In addition, an obvious exothermic peak appeared between 877 and 1000 °C. It is suggested that Al, Cr_2O_3 and SiC had an exothermic reaction in this interval. From the TG curve in Fig. 5, the mass of the sample first decreased and then increased. It is inferred that the decrease of sample
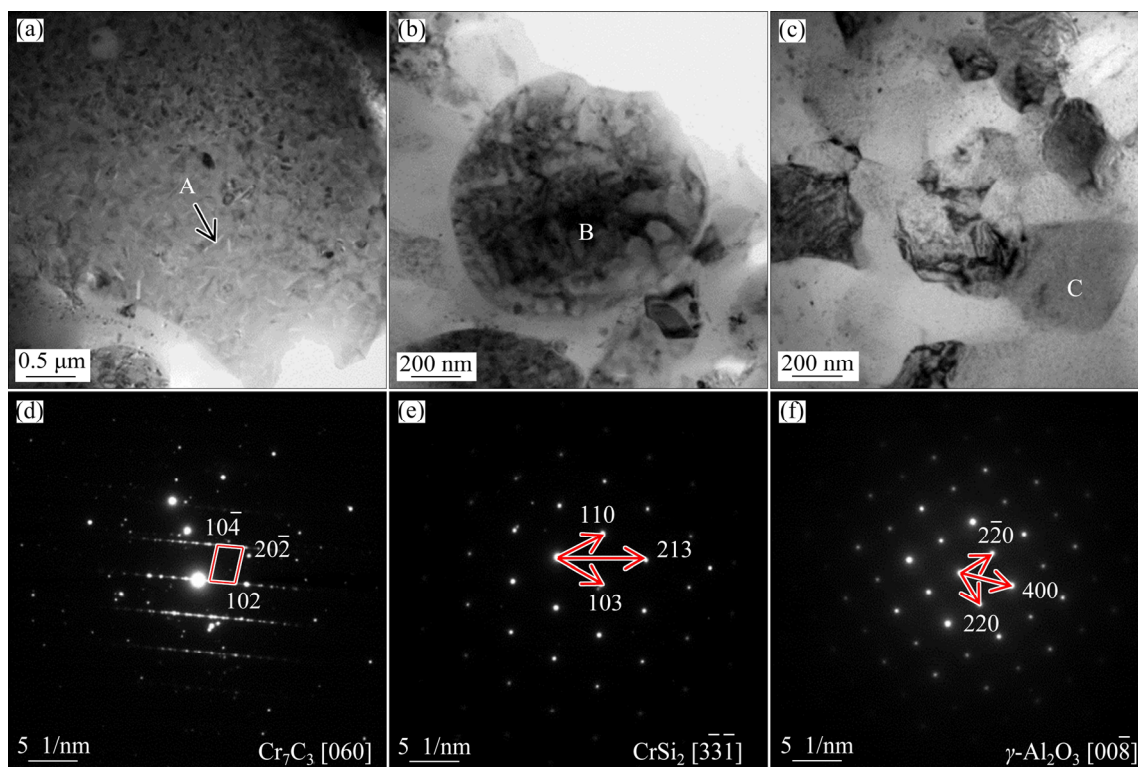

Fig. 3 TEM micrographs of Cr_7C_3 (a), $CrSi_2$ (b) and γ-Al_2O_3 (c) phases in Al−Cr_2O_3−SiC composite coating and selected area electron diffraction (SAED) patterns of Regions A (d), B (e) and C (f)
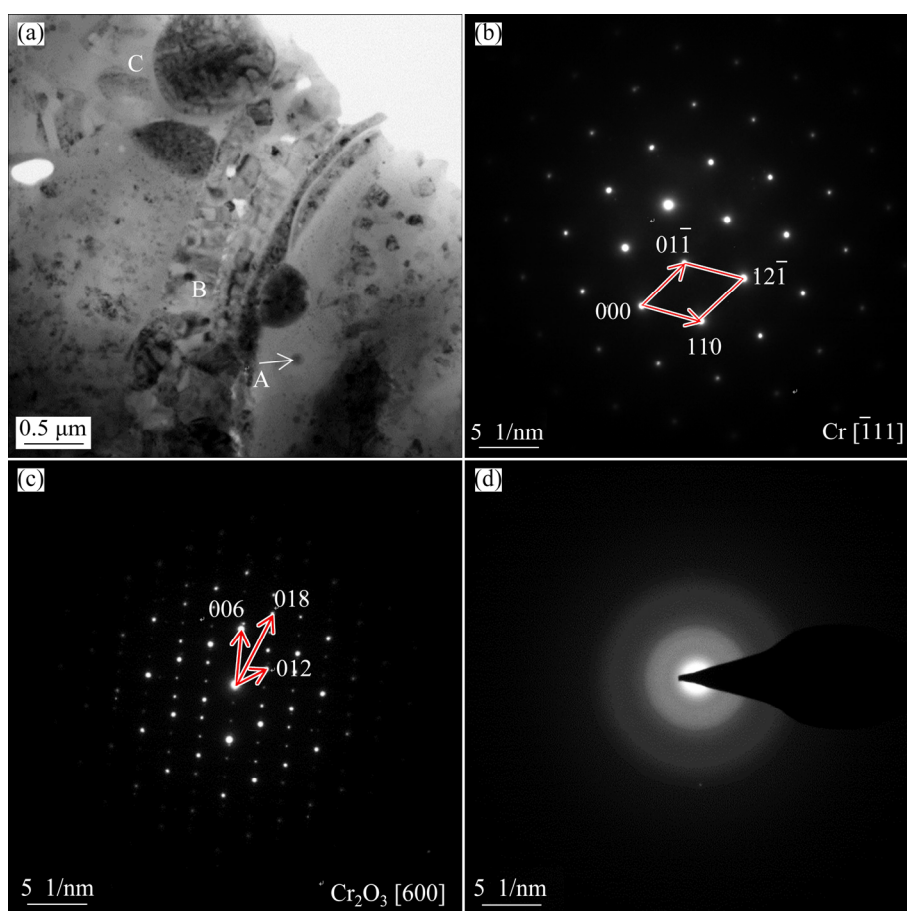
Fig. 4 TEM micrograph of Cr, Cr_2O_3 and amorphous phases in Al−Cr_2O_3−SiC composite coating (a) and selected area electron diffraction (SAED) patterns of Regions A (b), B (c) and C (d)
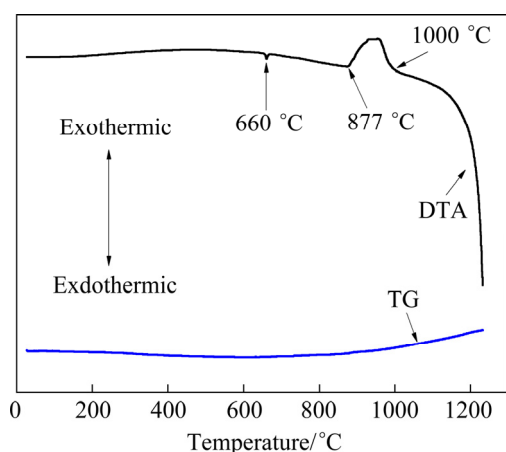

Fig. 5 DTA/TG curves of Al−Cr_2O_3−SiC composite powders

mass was caused by dehydration of composite powder and decomposition of binder. The increase of sample mass was related to the formation of new phases by the reaction of Al, Cr_2O_3 and SiC.

According to the position of the exothermic peak on the DTA curve of Al−Cr_2O_3−SiC system, four temperatures were selected to perform heat

treatment on the Al−Cr_2O_3−SiC composite powder. The heating rate of the heat treatment experiment was 10 °C/min, and the constant temperature treatment time was 30 min. Figure 6 shows the XRD patterns of heat-treated Al−Cr_2O_3−SiC composite powders. After constant temperature treatment at 800 °C, a small amount of Cr and Al_2O_3 were formed by the reaction of Al and Cr_2O_3. The reaction degree of Al and Cr_2O_3 increased after heat treatment at 900 °C, but the Cr produced by the reaction did not react with SiC. The reaction degree of Al and Cr_2O_3 in the Al−Cr_2O_3−SiC composite powder was further increased after the heat treatment at 1000 °C, and at the same time, the reaction-produced Cr reacted with SiC to produce Cr_7C_3, Cr_3Si and $CrSi_2$. The Al in the Al−Cr_2O_3−SiC powder disappeared after heat treatment at 1100 °C, and the final products were Cr_7C_3, $CrSi_2$, Cr_3Si, α-Al_2O_3, Cr_2O_3 and SiC. In summary, the reaction of Al and Cr_2O_3 in the Al−Cr_2O_3−SiC composite powder with a mass ratio of Al:Cr_2O_3:SiC of 23:65:12 occurs at 900 °C, and
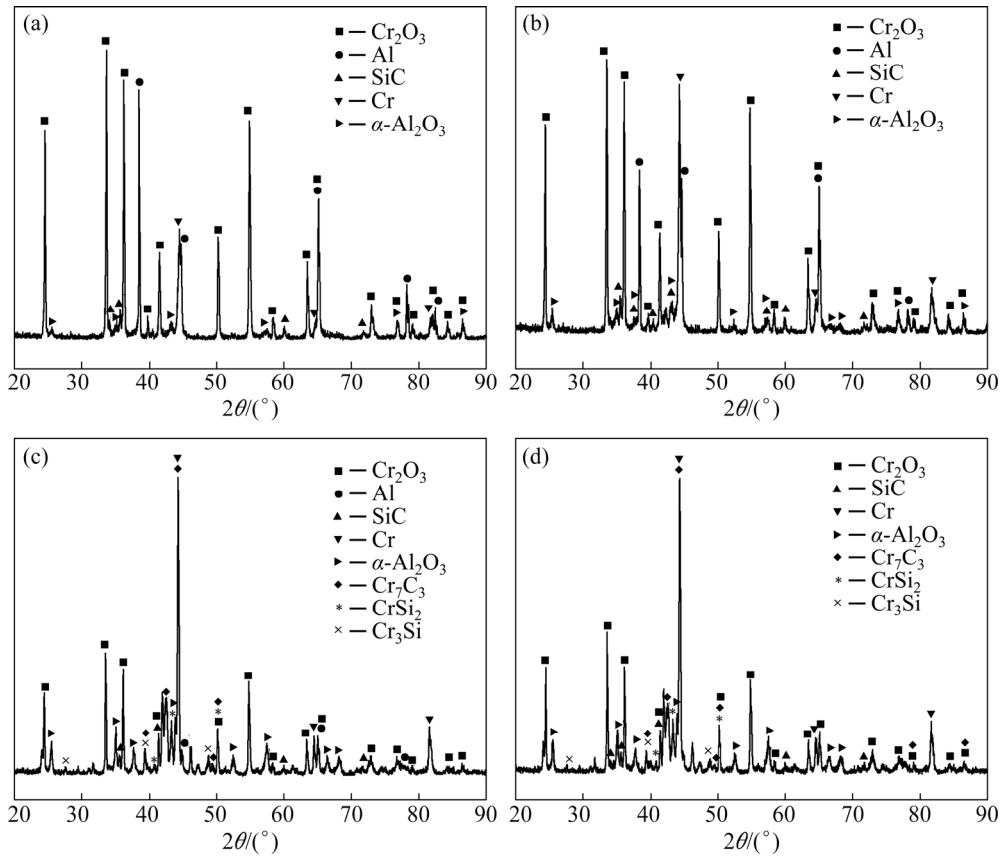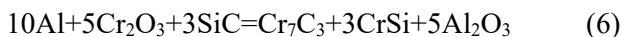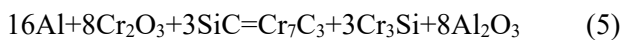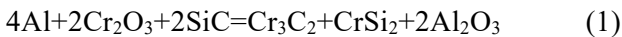
Fig. 6 XRD patterns of heat-treated Al−Cr$_2$O$_3$−SiC composite powders: (a) 800 °C, (b) 900 °C, (c) 1000 °C; (d) 1100 °C

the produced Cr and SiC start to react at 1000 °C. The reaction of the Al−Cr$_2$O$_3$−SiC system can be fully completed at 1100 °C.

Based on the above analysis, the possible reactions of Al−Cr$_2$O$_3$−SiC are as follows:

$$4Al+2Cr_2O_3+2SiC=Cr_3C_2+CrSi_2+2Al_2O_3 \quad (1)$$

$$18Al+9Cr_2O_3+4SiC=2Cr_3C_2+4Cr_3Si+9Al_2O_3 \quad (2)$$

$$10Al+5Cr_2O_3+4SiC=2Cr_3C_2+4CrSi+5Al_2O_3 \quad (3)$$

$$34Al+17Cr_2O_3+12SiC=4Cr_7C_3+6CrSi_2+17Al_2O_3 \quad (4)$$

$$16Al+8Cr_2O_3+3SiC=Cr_7C_3+3Cr_3Si+8Al_2O_3 \quad (5)$$

$$10Al+5Cr_2O_3+3SiC=Cr_7C_3+3CrSi+5Al_2O_3 \quad (6)$$

The Gibbs free energies of Reactions (1), (2), (3), (4), (5) and (6) were calculated according to the thermodynamic data. The curves of Gibbs free energy change with temperature for the reactions are shown in Fig. 7. From Fig. 7, the ΔG of Reactions (1), (2), (3), (4), (5) and (6) were all less than 0 in the range of 300−1500 K. This indicates that Reactions (1), (2), (3), (4), (5) and (6) were all possible within this range. By comparing these six
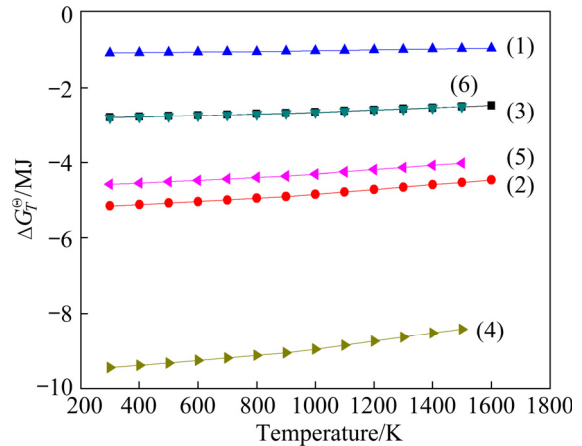

Fig. 7 Curves of Gibbs free energy change of multiple chemical reaction with temperature

reactions, it is found that the $\Delta G_T^{\ominus}$ value of Reaction (4) was the smallest, and thus Reaction (4) was more likely to occur. Figure 8 shows the calculation curves of the adiabatic temperature (T_{ad}) for Reactions (1), (2), (3), (4), (5) and (6). When the $\Delta H_{298}^{\ominus} + \sum n_i (H_T^{\ominus} - H_{298}^{\ominus})$ value of the curve is 0, the corresponding abscissa value is the adiabatic
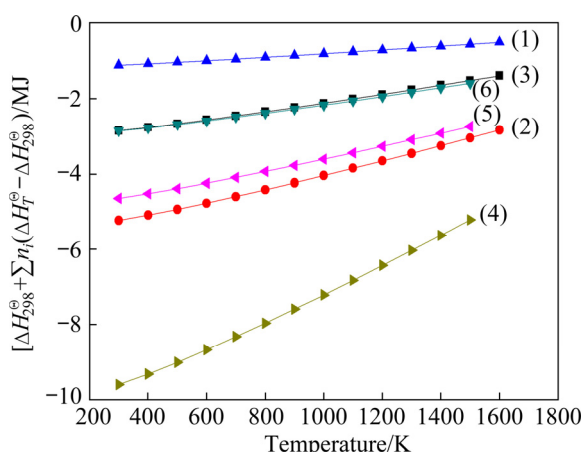
Fig. 8 Change curves of residual heat of multiple chemical reaction with temperature

temperature of the reaction. Due to insufficient thermodynamic data, the adiabatic temperature of each reaction cannot be directly obtained. But according to the curves corresponding to Reactions (1), (2), (3), (4), (5) and (6) in Fig. 8, adiabatic temperature can be estimated. The adiabatic temperatures of Reactions (1), (2), (3), (4), (5) and (6) were 2720, 3150, 2863, 2942, 3234 and 3028 K, respectively. The T_{ad} values of the six reactions are all higher than 1800 K, and thus the six reactions can be self-sustained.

3.2.2 Formation mechanism of $Cr_7C_3−CrSi_2−Al_2O_3$ and $Al−Cr_2O_3−SiC$ composite coatings

The plasma spray coating was formed by continuous accumulation of splats. Figure 9 shows the morphologies of the $Cr_7C_3−CrSi_2−Al_2O_3$ splat and $Al−Cr_2O_3−SiC$ splat. By comparison, it is found that the flattening degree of $Al−Cr_2O_3−SiC$ splat was higher than that of $Cr_7C_3−CrSi_2−Al_2O_3$. The reason is that the melting degree of $Al−Cr_2O_3−SiC$ composite powder was higher. This can explain

why the lamella of the as-prepared $Al−Cr_2O_3−SiC$ coating was thinner than that of $Cr_7C_3−CrSi_2−Al_2O_3$ coating. It can be found from Fig. 9 that pores and cracks appeared in the two splats. During the rapid solidification process, pores were formed because the droplets were too late to shrink. The reason for the cracks is that the stress caused by shrinkage can only be released by the formation of cracks.

The schematic diagram of the formation process of the plasma-sprayed $Cr_7C_3−CrSi_2−Al_2O_3$ composite coating is shown in Fig. 10. The formation process of plasma-sprayed $Cr_7C_3−CrSi_2−Al_2O_3$ coating can be regarded as a two-step process. First, the $Cr_7C_3−CrSi_2−Al_2O_3$ powder melts into droplets in the plasma jet. Subsequently, the molten or/and semi-melted droplets collide with the substrate, and then rapidly cool and solidify into a coating under the action of the plasma jet.

Figure 11 shows the schematic illustration of the formation process of the plasma-sprayed $Al−Cr_2O_3−SiC$ composite coating. The formation process of the $Al−Cr_2O_3−SiC$ coating can be regarded as a four-step process. (1) Al, which has a lower melting point, first melts, and then wraps Cr_2O_3 particles and SiC particles, so that each component is in complete contact and provides a good liquid phase environment for subsequent reactions. (2) Cr_2O_3 and Al undergo solid−liquid diffusion reaction, and the reaction produces Cr and Al_2O_3. At the same time, the heat released by the thermite reaction is superimposed on the heat of the plasma jet, which further promotes the progress of the reaction. (3) The Cr formed by Al and Cr_2O_3 reacts with SiC to produce chromium carbide and chromium silicide. (4) The molten droplets collide with the substrate to form $Al−Cr_2O_3−SiC$ coating under the action of the plasma jet.

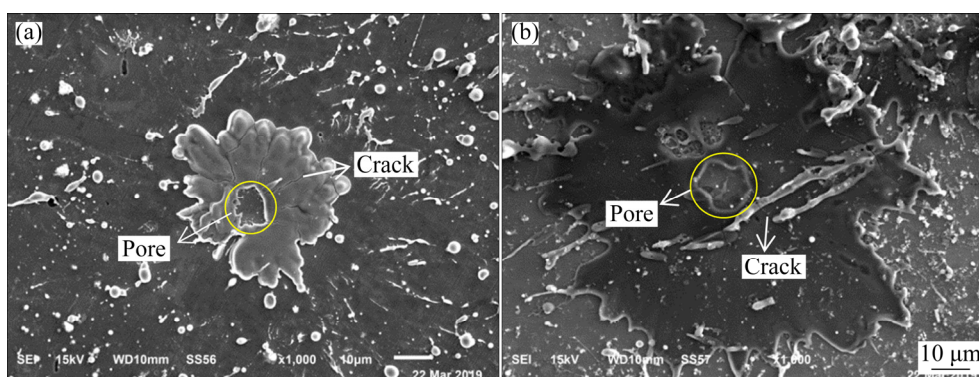**Fig. 9** Morphologies of $Cr_7C_3−CrSi_2−Al_2O_3$ splat (a) and $Al−Cr_2O_3−SiC$ splat (b) deposited on surface of polished substrate
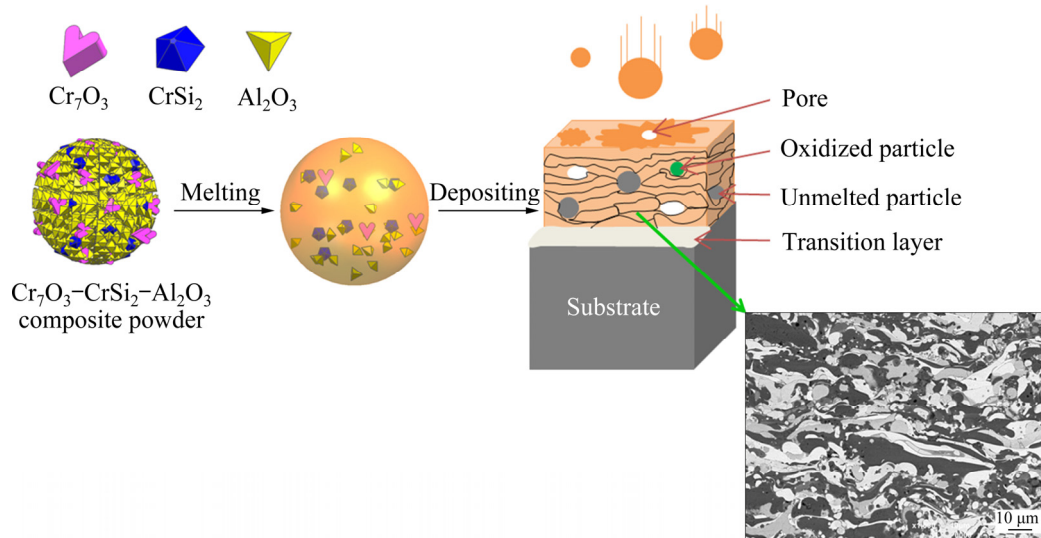
Fig. 10 Schematic diagram of formation mechanism of Cr_7C_3−$CrSi_2$−Al_2O_3 composite coating
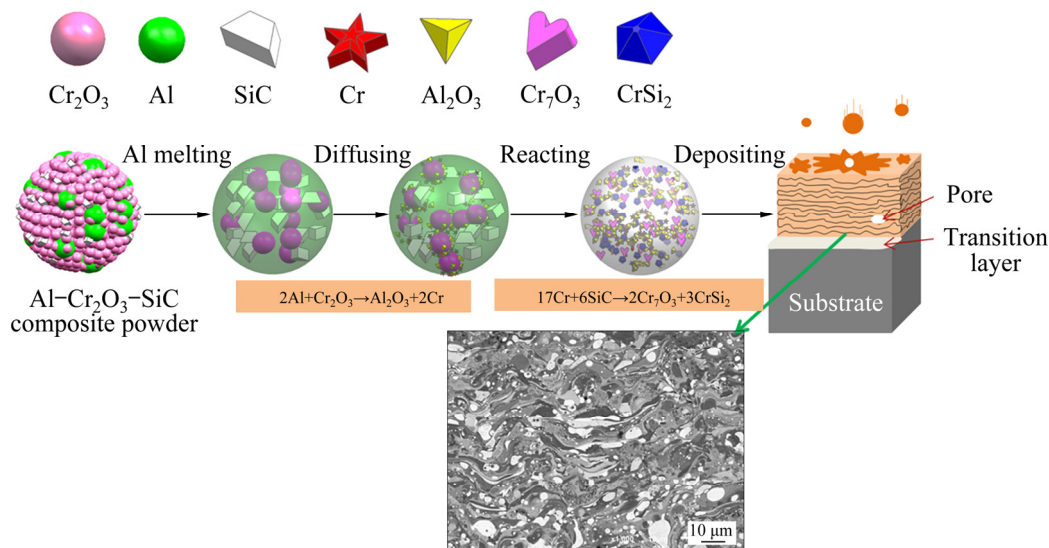
Fig. 11 Schematic diagram of formation mechanism of Al−Cr_2O_3−SiC composite coating

3.3 Properties of Cr_7C_3−$CrSi_2$−Al_2O_3 and Al−Cr_2O_3−SiC composite coatings

The microhardness of the coating is mainly affected by two factors [22]. The first factor is the organizational factor: the higher the density of the coating is, the less the defects (such as pores and cracks) are, which means the higher microhardness of the coating. In addition, the finer the grains in the coating are, the higher the hardness of the coating is. The second factor is the structural factor: the content and distribution uniformity of the hard phase in the coating affect the microhardness of the coating. The microhardness of the Al−Cr_2O_3−SiC coating ($HV_{0.1}$ 1432.2) was significantly higher than that of Cr_7C_3−$CrSi_2$−Al_2O_3 coating ($HV_{0.1}$ 1191.1).

The reason may be that the Al−Cr_2O_3−SiC coating had high density, fine grains and uniform microstructure distribution. As reported by WU et al [23], the average microhardness of the as-prepared Cr_7C_3 composite coating was HV 1050. The microhardness of the plasma-sprayed Cr_7C_3−$CrSi_2$ coating derived from Cr−SiC composite powders was $HV_{0.1}$ 1003.3 [16]. It can be seen that the Cr_7C_3−$CrSi_2$−Al_2O_3 and Al−Cr_2O_3−SiC composite coatings prepared in this work have higher microhardness. The non-uniform distribution of phases and the existence of defects in the composite coating make the microhardness of the composite coating present discrete distribution [24]. The Weibull distribution of the microhardness of

the Cr_7C_3−$CrSi_2$−Al_2O_3 and Al−Cr_2O_3−SiC coatings and their corresponding fitted lines are shown in Fig. 12. The slope of the fitted straight line can reflect the uniformity of the microstructure distribution of the coating. From Fig. 12, the slope of the Al−Cr_2O_3−SiC coating (8.97) was higher than that of the Cr_7C_3−$CrSi_2$−Al_2O_3 coating (7.29), so the microstructure distribution of Al−Cr_2O_3−SiC coating was more uniform.
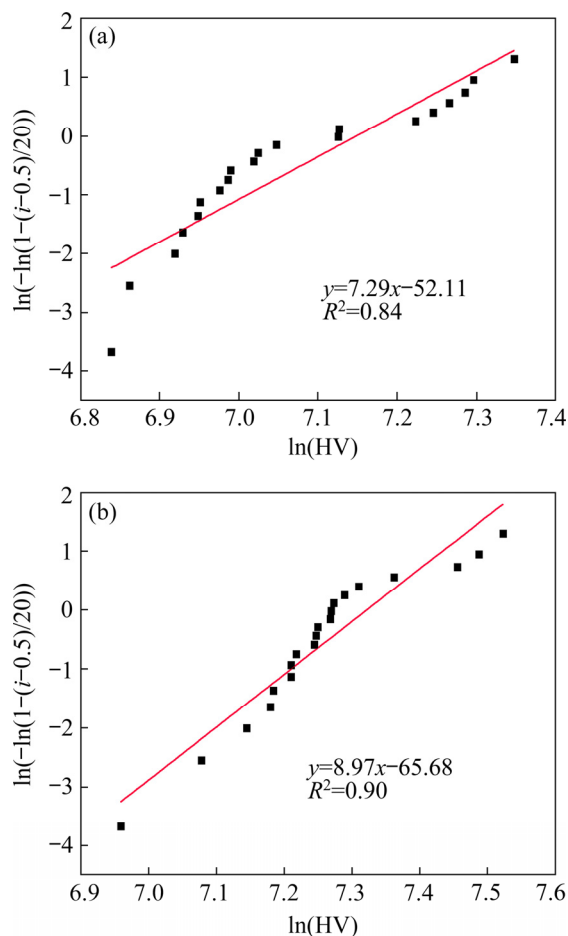

Fig. 12 Weibull distribution of microhardness and corresponding fitting lines of two composite coatings: (a) Cr_7C_3−$CrSi_2$−Al_2O_3; (b) Al−Cr_2O_3−SiC

By comparing the indentations of the two coatings, the diagonal length of the indentations of the Al−Cr_2O_3−SiC coating was smaller than that of the Cr_7C_3−$CrSi_2$−Al_2O_3 coating. It is again proven that the microhardness of the Al−Cr_2O_3−SiC coating was higher than that of the Cr_7C_3−$CrSi_2$−Al_2O_3 coating. From Fig. 13(a), significant crush was found at the edge of the Cr_7C_3−$CrSi_2$−Al_2O_3 coating indentation. However, the indentation profile of the Al−Cr_2O_3−SiC coating (Fig. 13(b)) was clear and there was no obvious damage.
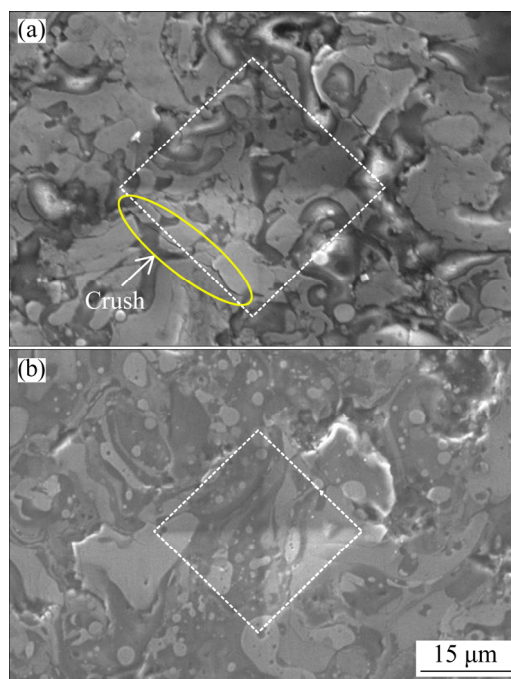

Fig. 13 Indentation morphologies of two composite coatings: (a) Cr_7C_3−$CrSi_2$−Al_2O_3; (b) Al−Cr_2O_3−SiC

Since no obvious propagation cracks were observed in the indentation morphologies of Cr_7C_3−$CrSi_2$−Al_2O_3 and Al−Cr_2O_3−SiC coatings, the toughness of the two coatings was analyzed again by the scratch method. Figure 14 shows the morphology of the middle section of the scratch and the end of the scratch of the two coatings. It can be seen from Fig. 14 that the scratch width and depth of the two coatings gradually increased with the increase of the load. By comparing the scratches of the two coatings, it was found that the internal cracks in the scratches of the Al−Cr_2O_3−SiC coating were shallower and the degree of damage at the edges was lower. The microstructure is one of the main factors affecting the scratch resistance of the coating. In general, the denser the coating is, the higher the hardness is, the better the toughness is, and the better the scratch resistance of the coating is [25].

From Fig. 15(a), there are partially melted regions in the Cr_7C_3−$CrSi_2$−Al_2O_3 coating. By comparing Figs. 15(a, b), it was found that the section of the Cr_7C_3−$CrSi_2$−Al_2O_3 coating was relatively flat, while the section of the Al−Cr_2O_3−SiC coating was uneven. Generally speaking, if the cross-section fluctuation of the coating is larger, the energy consumed in the fracture process of the coating is greater, and the fracture toughness of the
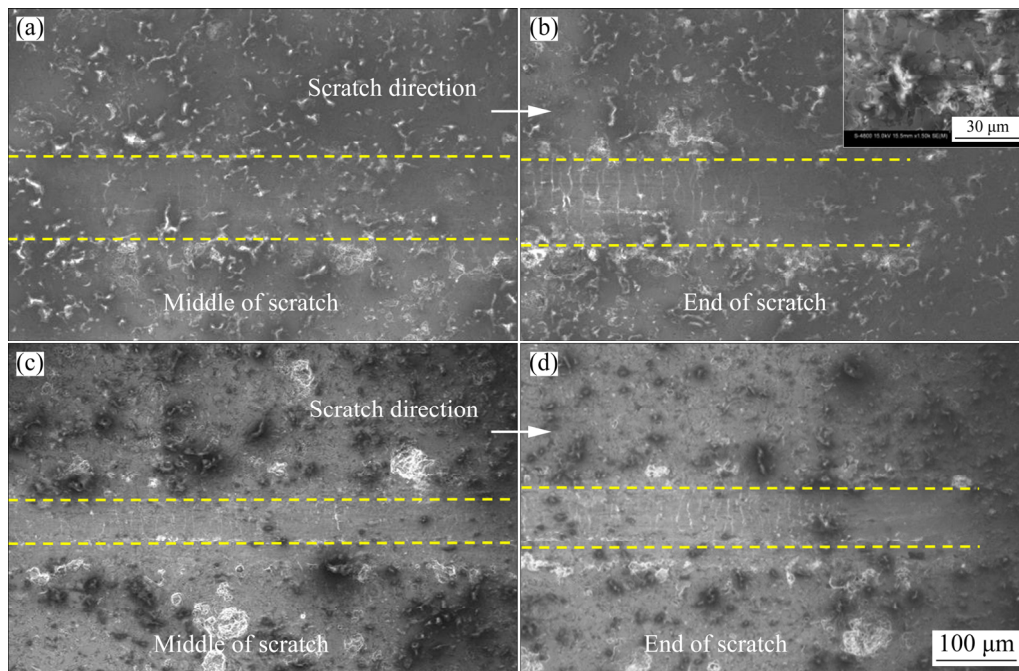
Fig. 14 SEM images of scratch morphology of two composite coatings: (a, b) $Cr_7C_3−CrSi_2−Al_2O_3$; (c, d) $Al−Cr_2O_3−SiC$
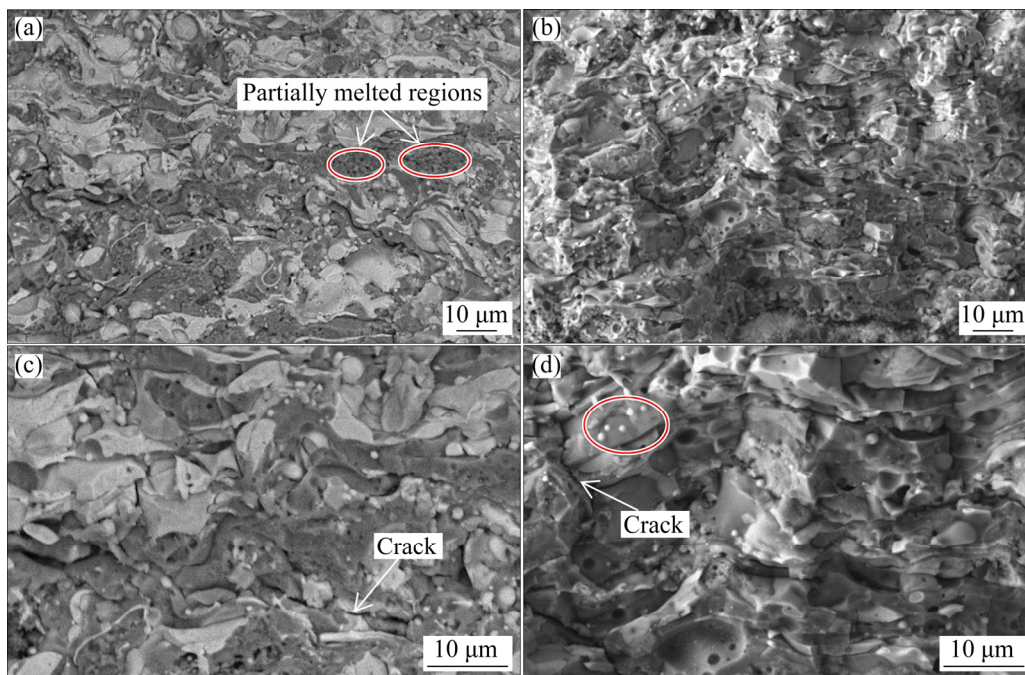
Fig. 15 SEM images of fracture morphologies of two composite coatings: (a, c) $Cr_7C_3−CrSi_2−Al_2O_3$; (b, d) $Al−Cr_2O_3−SiC$

coating is higher accordingly [26]. It can be found from Fig. 15(c) that interlayer cracks appeared in the section of the $Cr_7C_3−CrSi_2−Al_2O_3$ coating, which indicates that the interlayer bonding force of the $Cr_7C_3−CrSi_2−Al_2O_3$ coating was weak. Figure 15(d) shows that there was a tortuous longitudinal crack and some sub-micron particles on the cross-section of the $Al−Cr_2O_3−SiC$ coating.

The tortuous longitudinal cracks indicate that the fracture process of the $Al−Cr_2O_3−SiC$ coating was tortuous, and the fracture consumed more energy. Sub-micron particles may hinder crack propagation and pull-out during the coating fracture process, thereby playing a toughening role [27]. Therefore, the fracture toughness of $Al−Cr_2O_3−SiC$ coating was higher than that of $Cr_7C_3−CrSi_2−Al_2O_3$ coating.

The wear scar depth of the Al−Cr_2O_3−SiC coating was obviously lower than that of the Cr_7C_3−$CrSi_2$−Al_2O_3 coating, as shown in Fig. 16. The wear rate of Al−Cr_2O_3−SiC coating ($0.55×10^{-3}$ $mm^3/(N·m)$) was lower than that of Cr_7C_3−$CrSi_2$−Al_2O_3 coating ($0.76×10^{-3}$ $mm^3/(N·m)$). In summary, Al−Cr_2O_3−SiC coating had better wear resistance than Cr_7C_3−$CrSi_2$−Al_2O_3 coating. The reason is that the hard phase (Cr_7C_3, Al_2O_3, and $CrSi_2$) in the Al−Cr_2O_3−SiC coating had finer microstructure and more uniform distribution, the fracture of the Al−Cr_2O_3−SiC coating was not easy to occur during the wear process, and there was no large-scale laminar peeling.

Figure 17 shows the SEM images of the wear scar morphology of the two composite coatings. By comparing Figs. 17(a, b), it can be found that the wear scar of the Al−Cr_2O_3−SiC coating was
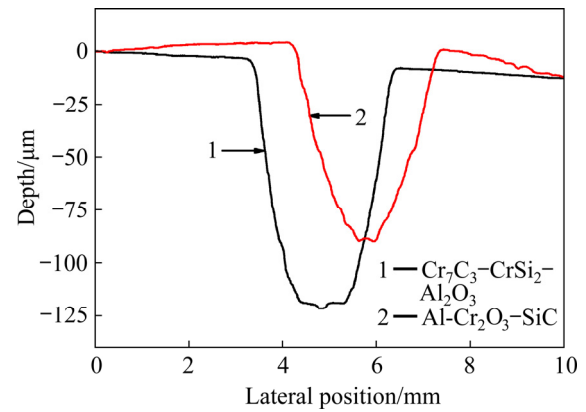
Fig. 16 Wear profiles of two composite coatings

shallower, and the smooth area of the Al−Cr_2O_3−SiC coating was larger. The smooth area is the deformation layer formed by the coating under pressure, while the rough area is the peeling pit
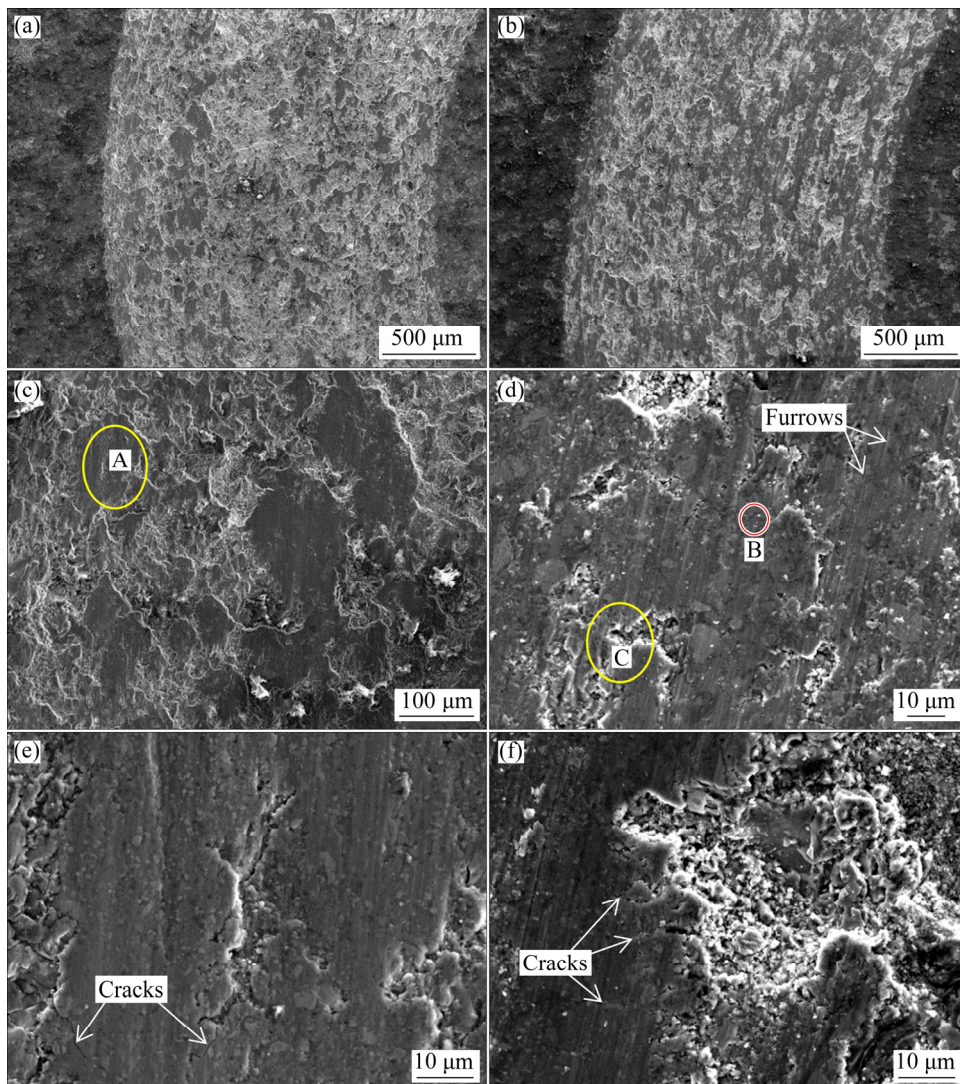
Fig. 17 SEM images of wear scar morphologies of two composite coatings: (a, c) Cr_7C_3−$CrSi_2$−Al_2O_3; (b, d) Al−Cr_2O_3−SiC; (e) High magnification of Region A in (c); (f) High magnification of Region C in (d)

formed by the peeling of the coating. It is again proven that the wear resistance of Al−Cr_2O_3−SiC coating was better than that of Cr_7C_3−$CrSi_2$−Al_2O_3 coating.

The wear scar morphology of the coatings was magnified and observed to analyze the wear mechanism of the coatings. From Fig. 17(c), the wear scar of the Cr_7C_3−$CrSi_2$−Al_2O_3 coating presented a stepladder-like morphology. A large shear stress was produced on the surface of the coating during the wear process. Under the combined action of shear stress and compressive stress, microcracks appeared on the surface and internal defects of the coating. The microcracks propagated continuously between the layers with weak bonding force, which eventually caused the spalling of the coating and the formation of step-like morphology. It can be found from Fig. 17(e) that the cracks in the Cr_7C_3−$CrSi_2$−Al_2O_3 coating gradually expanded and the coating was peeled off. It is inferred that the wear mechanism of Cr_7C_3−$CrSi_2$−Al_2O_3 coating under sliding wear was mainly adhesive wear. Different from Cr_7C_3−$CrSi_2$−Al_2O_3 coating, Al−Cr_2O_3−SiC coating had relatively clear surface grooves and wear debris (Region B), but the wear mark depth was very shallow (Fig. 17(d)). It can be seen from Fig. 17(f) that the rough area of the Al−Cr_2O_3−SiC coating was formed by the smooth structure falling-off with the continuous expansion of cracks. With the wear going on, the shear deformation caused stress concentration, which led to the formation of microcracks. These microcracks continued to expand and eventually caused the coating to peel off and form spalling pits. Therefore, it is considered that the wear mechanism of Al−Cr_2O_3−SiC coating was mainly abrasive wear.

4 Conclusions

(1) The phase compositions of the Cr_7C_3−$CrSi_2$−Al_2O_3 coating derived from Cr_7C_3−$CrSi_2$−Al_2O_3 composite powders were Cr_7C_3, $CrSi_2$, γ-Al_2O_3, α-Al_2O_3, Cr_3C_2, CrSi and Cr_2O_3. The phase compositions of as-prepared Cr_7C_3−$CrSi_2$−Al_2O_3 coating derived from Al−Cr_2O_3−SiC composite powders were Cr_7C_3, γ-Al_2O_3, $CrSi_2$, CrSi, Cr, Cr_2O_3 and SiC. The Cr_7C_3−$CrSi_2$−Al_2O_3 coating obtained by Al−Cr_2O_3−SiC composite powders had thinner lamella, smaller grain size and more

tortuous interlayer interfaces than Cr_7C_3−$CrSi_2$−Al_2O_3 coating derived by Cr_7C_3−$CrSi_2$−Al_2O_3 composite powders.

(2) The formation mechanism of the plasma-sprayed Cr_7C_3−$CrSi_2$−Al_2O_3 coating derived from Al−Cr_2O_3−SiC composite powders can be described by melting−reaction−deposition solidification. The reaction process was as follows: firstly, Cr_2O_3 and Al reacted to form Al_2O_3 and Cr, and then, Cr generated by reaction reacted with SiC to form chromium carbide and chromium silicide. The reaction of the Al−Cr_2O_3−SiC system can be fully completed at 1100 °C.

(3) Compared with the Cr_7C_3−$CrSi_2$−Al_2O_3 coating obtained by traditional spraying, the Cr_7C_3−$CrSi_2$−Al_2O_3 coating obtained by plasma spraying Al−Cr_2O_3−SiC composite powders had higher density, higher microhardness (increased by 20%), better fracture toughness and lower wear rate (reduced by 28%).

Acknowledgments

References

[1]   SINGH B, ZAFAR S. Effect of microwave exposure time on microstructure and slurry erosion behavior of Ni + 20%Cr_7C_3 composite clads [J]. Wear, 2019, 426/427: 491−500.

[2]   WANG Xing-yu, YANG Wei, SHAO Yu-xuan, YANG Yong, YANG Zhen-long, WANG Yan-wei, CUI Yu-hang, MA Yu-duo, SUN Wen-wei, LI Wei. Effect of nano-Al_2O_3 on the microstructure and properties of NbB_2−NbC composite coatings prepared by plasma spraying [J]. Journal of the American Ceramic Society, 2022, 105: 712−727.

[3]   FRANGINI S, MASCI A, BARTOLOMEO A D. Cr_7C_3-based cermet coating deposited on stainless steel by electrospark process: structural characteristics and corrosion behavior [J]. Surface and Coatings Technology, 2002, 149: 279−286.

[4]   LI Wei, WANG Lei, YANG Yong, ZHANG Xia, CUI Yu-hang, MA Yu-duo, WANG Yan-wei, SUN Wen-wei, WANG Xing-yu, SHAO Yu-xuan. Microstructure and properties of niobium carbide composite coatings prepared by plasma spraying [J]. Ceramics International, 2021, 47: 33338−33352.

[5]   WANG Pei-pei, LI He-jun, YUAN Rui-mei, KONG Jing-an, LI Tao, ZHANG Yu-lei. A $CrSi_2$−HfB_2−SiC coating providing oxidation and ablation protection over 1973 K for

SiC coated C/C composites [J]. Corrosion Science, 2020, 167: 108536.

[6]   MIAO Chun-mao, SUN Wei, XIONG Xiang, ZHANG Hong-bo, XU Yong-long. Effect of Fe content on microstructure and ablation properties of Fe$_x$Si$_y$ modified C/C−ZrC−SiC composites [J]. The Chinese Journal of Nonferrous Metals, 2021, 31: 836−846. (in Chinese)

[7]   LIU Fei, LI He-jun, GU Sheng-yue, YAO Xi-yuan, FU Qian-gang. Microstructure and oxidation property of CrSi$_2$−ZrSi$_2$−Y$_2$O$_3$/SiC coating prepared on C/C composites by supersonic atmosphere plasma spraying [J]. Surface and Coatings Technology, 2019, 374: 966−974.

[8]   JIA Jian-gang, ZHANG Bo, LIU Di-qiang, LIU Shun-wei, JI Gen-shun, JI Rui-fang. Effects of Al$_2$O$_3$ coating induced structural and mechanical changes of C/C composites [J]. Journal of Alloys and Compounds, 2020, 818: 152847.

[9]   MA Yu-duo, LI Wei, GUO Ming-yan, YANG Yong, CUI Yu-hang, SUN Wen-wei, DONG Yan-chun, YAN Dian-ran. TiC−TiSi$_2$−Al$_2$O$_3$ composite coatings prepared by spray drying, heat treatment and plasma spraying [J]. Journal of Alloys and Compounds, 2021, 857: 158221.

[10]   WANG Xiao-long, SHAO Yu-xuan, GUO Ming-yan, YANG Yong, MA Yu-duo, CUI Yu-hang, SUN Wen-wei, DONG Yan-chun, YAN Dian-ran. Comparison of plasma sprayed NbB$_2$−NbC coatings obtained by ex-situ and in-situ approaches [J]. Journal of the European Ceramic Society, 2021, 41: 5088−5099.

[11]   ZHANG Chao, LIU Gui-fang, LIU Ke-wei, WU Kai-di. ZnO$_{1−x}$ coatings deposited by atmospheric plasma spraying for room temperature ppb-level NO$_2$ detection [J]. Applied Surface Science, 2020, 528: 147041.

[12]   ZOU Ke, ZOU Jian-peng, DENG Chun-ming, LIU Min, LIU Xue-zhang, ZHAO Rui-min, LI Shun-hua, ZHU Ren-bo, GAO Di. Preparation and properties of supersonic atmospheric plasma sprayed TiB$_2$−SiC coating [J]. Transactions of Nonferrous Metals Society of China, 2021, 31: 243−254.

[13]   ZHANG Li-zheng, ZHAO Zhan-yong, BAI Pei-kang, DU Wen-bo, LI Yu-xin, YANG Xiao, WANG Qin. In-situ synthesis of TiC/graphene/Ti6Al4V composite coating by laser cladding [J]. Materials Letters, 2020, 270: 127711.

[14]   HUAN Yu-chun, WU Kai-di, LI Chang-jiu, LIAO Han-lin, DEBLIQUY M, ZHANG Chao. Micro−nano structured functional coatings deposited by liquid plasma spraying [J]. Journal of Advanced Ceramics, 2020, 9: 517−534.

[15]   ZHANG Dan, CUI Xiu-fang, JIN Guo, FENG Xiang-ru, LU Bing-wen, SONG Qi-liang, YUAN Chen-feng. Effect of in-situ synthesis of multilayer graphene on the micro-structure and tribological performance of laser cladded Ni-based coatings [J]. Applied Surface Science, 2019, 495: 143581.

[16]   MA Yu-duo, GUO Ming-yan, LI Wei, YANG Yong, GAO Peng-yue, CUI Yu-hang, SUN Wen-wei, WANG Yan-wei, WANG Lei, DONG Yan-chun. Microstructure and properties of Cr$_7$C$_3$−CrSi$_2$ composite coatings prepared by plasma spraying [J]. Surface and Coatings Technology, 2021, 412: 127011.

[17]   ZHANG Qi, YANG Yong, REN Xian-xing, YANG Zhen-long, GAO Peng-yue, ZHAO Ce-ce, CHU Zhen-hua, WANG Lei, LI Jiao, DONG Yan-chun. Microstructure and properties of composite coatings prepared by plasma spraying ZrO$_2$−B$_2$O$_3$−Al composite powders [J]. Journal of Alloys and Compounds, 2018, 740: 124−131.

[18]   XU Jia-ying, ZOU Bing-lin, TAO Shun-yan, ZHANG Meng-xian, CAO Xue-qiang. Fabrication and properties of Al$_2$O$_3$−TiB$_2$−TiC/Al metal matrix composite coatings by atmospheric plasma spraying of SHS powders [J]. Journal of Alloys and Compounds, 2016, 672: 251−259.

[19]   GOBERMAN D, SOHN Y H, SHAW L, JORDAN E, GELL M. Microstructure development of Al$_2$O$_3$−13wt.%TiO$_2$ plasma sprayed coatings derived from nanocrystalline powders [J]. Acta Materialia, 2002, 50: 1141−1152.

[20]   WANG Jun-zhong, MANGA K K, BAO Qiao-liang, LOH K P. High-yield synthesis of few-layer graphene flakes through electrochemical expansion of graphite in propylene carbonate electrolyte [J]. Journal of the American Chemical Society, 2011, 133: 8888−8891.

[21]   ZOU Bing-lin, SHEN Ping, CAO Xue-qiang, JIANG Qi-chuan. Reaction path of the synthesis of α-Al$_2$O$_3$−TiC−TiB$_2$ in an Al−TiO$_2$−B$_4$C system [J]. International Journal of Refractory Metals and Hard Materials, 2011, 29: 591−595.

[22]   PAWLOWSKI L. Strategic oxides for thermal spraying: Problems of availability and evolution of prices [J]. Surface and Coatings Technology, 2013, 220: 14−19.

[23]   WU Qian-lin, LI Wen-ge, ZHONG Ning, GANG Wu, WANG Hai-shan. Microstructure and wear behavior of laser cladding VC-Cr$_7$C$_3$ ceramic coating on steel substrate [J]. Materials & Design, 2013, 49: 10−18.

[24]   MA Yu-duo, WANG Xing-yu, WANG Xiao-long, YANG Yong, CUI Yu-hang, SUN Wen-wei. In-situ TiC−Ti$_5$Si$_3$−SiC composite coatings prepared by plasma spraying [J]. Surface and Coatings Technology, 2020, 404: 126484.

[25]   CAO Fu-yang, MUNROE P, ZHOU Zhi-feng, XIE Zong-han. Mechanically robust TiAlSiN coatings prepared by pulsed-DC magnetron sputtering system: Scratch response and tribological performance [J]. Thin Solid Films, 2018, 645: 222−230.

[26]   YANG Yong, YAN Dian-ran, DONG Yan-chun, WANG Lei, CHEN Xue-guang, ZHANG Jian-xin, HE Ji-ning, LI Xiang-zhi. In situ nanostructured ceramic matrix composite coating prepared by reactive plasma spraying micro-sized Al−Fe$_2$O$_3$ composite powders [J]. Journal of Alloys and Compounds, 2011, 509: 90−94.

[27]   DAI Xue-rui, YAN Dian-ran, YANG Yong, CHU Zhen-hua, CHEN Xue-guang, SONG Jin-song. In situ (Al,Cr)$_2$O$_3$−Cr composite coating fabricated by reactive plasma [J]. Ceramics International, 2017, 43: 6340−6344.

等离子喷涂 Cr$_7$C$_3$−CrSi$_2$−Al$_2$O$_3$ 涂层的
显微组织、形成机制和性能

马玉夺 [1]，茹沛文 [1]，王 磊 [1]，杨 勇 [1]，高鹏悦 [1]，

王彦伟 [1]，崔宇航 [1]，孙文韦 [1]，王星宇 [1]，王 亮 [2]

1. 河北工业大学 天津市材料层状复合与界面控制技术重点实验室，电工装备可靠性与智能化国家重点实验室，
材料科学与工程学院，河北省新型功能材料重点实验室，天津 300401；
2. 中国科学院 上海硅酸盐研究所 集成计算材料研究中心，上海 201899

摘　要：采用等离子喷涂 Cr$_7$C$_3$−CrSi$_2$−Al$_2$O$_3$ 和 Al−Cr$_2$O$_3$−SiC 复合粉分别制备 Cr$_7$C$_3$−CrSi$_2$−Al$_2$O$_3$ 复合涂层。对比研究等离子喷涂所得两种 Cr$_7$C$_3$−CrSi$_2$−Al$_2$O$_3$ 复合涂层的显微组织、形成机制和性能，并探索 Al−Cr$_2$O$_3$−SiC 体系的反应机理。结果表明，等离子喷涂 Al−Cr$_2$O$_3$−SiC 复合粉所得涂层具有更薄的片层、更曲折的层间界面，而且涂层中原位合成的 Cr$_7$C$_3$、CrSi$_2$ 和 Al$_2$O$_3$ 均为纳米晶。与等离子喷涂 Cr$_7$C$_3$−CrSi$_2$−Al$_2$O$_3$ 复合粉制备的 Cr$_7$C$_3$−CrSi$_2$−Al$_2$O$_3$ 涂层相比，等离子喷涂 Al−Cr$_2$O$_3$−SiC 复合粉所得 Cr$_7$C$_3$−CrSi$_2$−Al$_2$O$_3$ 涂层具有更高的致密度、更高的显微硬度(提高 20%)、更好的断裂韧性和更低的磨损率(降低 28%)。

关键词：等离子喷涂；原位合成；纳米结构；强韧化；耐磨性

(Edited by Bing YANG)